

# Chapter 6

## Validation of Flash Flood Simulations Using Satellite Images and Community-Based Observations— Impact of Infiltration and Small-Scale Topographical Features



Franziska Tügel, Ahmed Hadidi, Ilhan Özgen-Xian, Jingming Hou,  
and Reinhard Hinkelmann

**Abstract** This work is aimed at investigating flash floods in the region of El Gouna, Egypt, by using a 2D robust shallow-water model that incorporates the Green-Ampt model to find the most realistic infiltration setting for this desert area. The results of different infiltration settings are compared to inundation areas observed from LANDSAT 8 images as well as to community-based information and photographs to validate the results despite scarce data availability. The model tends to overestimate infiltration in the study area if tabulated Green-Ampt parameters for the dominant soil texture class are considered. Specifically, bare soils with no vegetation tend to develop a surface crust, leading to significantly decreased infiltration rates during heavy rainfalls. Comparing the results of different infiltration settings with the observed data showed that the crust approach or the consideration of sandy clay loam instead of sand led to more plausible results for

---

F. Tügel (✉) · R. Hinkelmann

Chair of Water Resources Management and Modeling of Hydrosystems, Technische  
Universität Berlin, Straße des 17. Juni 135, 10623 Berlin, Germany  
e-mail: [franziska.tuegel@wahyd.tu-berlin.de](mailto:franziska.tuegel@wahyd.tu-berlin.de)

R. Hinkelmann

e-mail: [reinhard.hinkelmann@wahyd.tu-berlin.de](mailto:reinhard.hinkelmann@wahyd.tu-berlin.de)

A. Hadidi

Department of Applied Geosciences, GÜtech German University of Technology, Muscat,  
Oman

I. Özgen-Xian

Geochemistry Department, EESA, Lawrence Berkeley National Laboratory, Berkeley, CA,  
USA

e-mail: [iozgen@lbl.gov](mailto:iozgen@lbl.gov)

J. Hou

School of Water Resources and Hydro-Power Engineering, Xi'an University of Technology,  
Xi'an, China

e-mail: [jingming.hou@xaut.edu.cn](mailto:jingming.hou@xaut.edu.cn)

© The Author(s) 2022

T. Sumi et al. (eds.), *Wadi Flash Floods*, Natural Disaster Science and Mitigation  
Engineering: DPRI Reports, [https://doi.org/10.1007/978-981-16-2904-4\\_6](https://doi.org/10.1007/978-981-16-2904-4_6)

the considered study area than those obtained using the values for sand from two different sources in the literature. Furthermore, small-scale structures, which are not appropriately captured in the original digital surface model, but significantly affect the resulting flow field, have been included based on the available information leading to much more plausible results.

**Keywords** Shallow water equations · Hydroinformatics modeling system · Green-Ampt Model · Data scarcity · Landsat-8 · Egypt

## 6.1 Introduction

Flash floods generated by heavy rainfall events occur all over the world, even in desert areas. As they occur very suddenly and have destructive power, flash floods can affect highly developed cities as well as areas with poor infrastructure. This emphasizes how challenging it is to deal with such events. As climate change and enhanced urbanization might lead to increased intensities and frequencies of such events, appropriate mitigation and adaptation measures will become even more important. In arid regions such as the Eastern Desert of Egypt, flash floods are often caused by heavy rainfall in wadi catchments, where high rainfall amounts from a large area quickly accumulate in the wadi streams. Often, cities and settlements are located in the downstream regions of normally dry wadi catchments, and during rare flash flood events, these cities and settlements are immediately at high risk of flooding. Flash floods also affect the Red Sea region of Egypt almost every year, leading to damage to infrastructure and properties and endangering human lives. This work presents a 2D shallow-water model setup for El Gouna, a town of approximately 15,000 inhabitants located along the Red Sea coast of Egypt. The model can be used to analyze the flood areas generated from different rainfall events and to investigate different structural mitigation measure scenarios, such as retention basins and drainage channels. In previous work, a sensitivity analysis on a simplified catchment was carried out, and the results showed that in addition to other parameters, such as friction and rain intensity, infiltration has a strong influence on runoff at the outlet of the catchment (Tügel et al. 2018). In Tügel et al. (2020a), the impacts of infiltration under different parameter sets as well as under different mitigation measure scenarios for the city of El Gouna were studied, and infiltration was represented for different extreme rainfall events. As Hou et al. (2020) showed that the temporal storm resolution plays an important role in obtaining reliable simulation results of inundated areas, a temporal rainfall distribution was incorporated in the model used to study flash floods in El Gouna instead of a simplified approach consisting of a constant average rain intensity, as used in earlier studies, e.g., Tügel et al. (2020a).

The calibration and validation of flash flood models are commonly challenging, as in most cases, no direct measurements of water depths or flow velocities are available due to the sudden occurrence of heavy rainfall. Furthermore, the spatial

distribution of flash floods over a wide land surface instead of at fixed points, as during river floods, exacerbates the challenge of obtaining direct measurements. Therefore, other data sources must be considered to obtain estimations of flood extent and water depth to check the plausibility of simulation results. A useful and widely available source for detecting land cover changes and flood areas are remotely sensed multispectral images, for example, from the Landsat-8 or Sentinel-2 satellites; however, due to their rather coarse temporal resolutions of several days up to weeks, their usability is limited when considering relatively short flood events such as flash floods. In recent years, community-based, crowd-sourced data or so-called citizen science approaches have been used in different studies, for example, for studies on the hydrological modeling of ungauged catchments and flash floods (Starkey et al. 2017) and studies aiming to validate the results of city-scale 2D flood simulations (Yu et al. 2016). Smith et al. (2017) assessed the usefulness of social media for flood risk management, and Liang et al. (2017) investigated the potential contribution of crowd-sourced data such as photographs and messages to real-time flood forecasting.

Infiltration excess represents the main contributor to runoff generation during storm events in arid areas. Especially in rural areas and urban green spaces, infiltration losses cannot be neglected. An appropriate representation of infiltration during heavy rainfall events is important to include the runoff generation in hydrodynamic models and for calculating water depths and flooding areas more realistically. Additionally, due to the increasing interest in sustainable urban drainage systems (SUDS) (e.g., Vergroesen et al. 2014; Ghazal 2018; Hou et al. 2019), the appropriate consideration of infiltration in 2D hydrodynamic rainfall-runoff models is also of great interest for the accurate assessment of the effectiveness of decentralized stormwater management measures such as infiltration basins and trenches. The Green-Ampt model (Green and Ampt 1911) is often used to calculate time-dependent infiltration rates; for example, it is often used in hydrological catchment models. However, only a few studies have coupled a 2D shallow-water model with the Green-Ampt model, such as Esteves et al. (2000) and Xing et al. (2019), which showed the general capability of these methods to simulate rainfall runoff and infiltration processes.

For real-world applications, it is often difficult to estimate the Green-Ampt parameters in terms of the hydraulic conductivity, capillary suction head at the wetted front, and effective porosity of a catchment area, in addition to the initial soil water content of the soil. If runoff measurements are available, the Green-Ampt parameters are often considered as calibration parameters (e.g., Fernández-Pato et al. 2016; Ni et al. 2020). For ungauged areas or during flash floods, direct measurements are usually unavailable, and different methods to estimate the Green-Ampt parameters have evolved and been investigated in recent decades. One well-known contribution is the work of Rawls et al. (1983), in which average parameter sets dependent on the soil texture class and soil horizon were derived from 5000 soil samples. In the manual of the modeling software company Innowat (2019), other average values are recommended to be used to estimate the

Green-Ampt parameters if no measurements are available, and these estimations refer to different sources, such as Akan (1993).

During heavy rainfall events, soil surfaces can become clogged, which leads to reduced infiltration rates. In particular, on bare, unprotected soils without vegetation in arid regions such as the study area, the kinetic energy of raindrops can cause the formation of a surface seal or crust (Morin and Benyamini 1977; Müller 2007; Nciizah and Wakindiki 2015). Such layers have been observed to be approximately 1 to 5 mm thick (Tackett and Pearson 1965; Sharma et al. 1980). A modified Green-Ampt model in which the hydraulic conductivity is calculated as the effective hydraulic conductivity of the crust and subcrust soil is one simple approach that can be used to account for the effects of a surface crust (Brakensiek and Rawls 1983; Esteves et al. 2000; Nciizah and Wakindiki 2015).

In this study, the results of flash flood simulations of the event that occurred on March 09, 2014 in El Gouna are validated by Landsat-8 images as well as community-based photographs and statements. The most suitable infiltration settings were determined, while the tabulated Green-Ampt parameters from two different sources were considered with and without the consideration of a surface crust of reduced hydraulic conductivity, following the approach of Brakensiek and Rawls (1983). Furthermore, the topographical data were checked due to poor agreement of the model results with the observed data at some locations for the late timesteps. Three major modifications in the original digital surface model (DSM) based on observations from satellite images and photographs were proposed to improve the model results.

## 6.2 Methods and Materials

### 6.2.1 *Shallow Water Flow Model*

To set up a 2D shallow water flow model of the study area, the hydroinformatics modeling system (hms) was used; this system is an in-house software of the Chair of Water Resources Management and Modeling of Hydrosystems, Technische Universität Berlin (Simons et al. 2012, 2014; Busse et al. 2012). In the system, different laws are implemented to calculate the bottom friction, and rainfall and infiltration can be considered for each cell individually through sink/source terms in the mass balance equation. In this study, the turbulent viscosity,  $\nu_t$ , is set to zero as turbulent effects can usually be neglected in rainfall-runoff simulations. The bottom friction is calculated with Manning's law. The general form of the conservation laws is spatially discretized with a cell-centered finite-volume method, and an explicit forward Euler method is used for the time discretization. The conserved variables,  $q$ , for the new time level,  $n + 1$ , are calculated as shown in Eq. (6.1):

$$\mathbf{q}^{n+1} = \mathbf{q}^n - \frac{\Delta t}{A} \sum_k \mathbf{F}_k^n \cdot \mathbf{n}_k l_k + \Delta t \mathbf{s}^n \quad (6.1)$$

where  $n + 1$  and  $n$  denote the new and old time levels, respectively;  $\mathbf{q}$  is the vector of conserved variables;  $\mathbf{F}$  is the flux vector over edge  $k$ ;  $\mathbf{s}$  is the vector of source terms;  $k$  is the index of a face of the considered cell. The timestep is denoted with  $\Delta t$ ;  $A$  is the area of the considered cell;  $\mathbf{n}$  is the normal vector pointing outward from the face;  $l$  is the length of the face.

Equation (6.1) is solved with a second-order MUSCL scheme (Hou et al. 2013). As rainfall-runoff simulations usually deal with small water depths over complex topography and are associated with propagating wet-dry fronts, flow transitions, and high gradients, robust numerical methods are required to prevent numerical problems and instabilities. The implemented HLLC Riemann solver used to compute the fluxes over the cell edges is able to handle discontinuities in the flow field. A total variation diminishing scheme including different slope limiters is used to avoid spurious oscillations (Hou et al. 2013; Özgen et al. 2014). The water depth threshold necessary to consider a cell as dry was set to  $10^{-6}$  m, and at high gradients, the scheme switches from second-order to first-order accuracy (Hou et al. 2013; Murillo et al. 2009).

## 6.2.2 Infiltration

Infiltration processes were represented with the Green-Ampt model. In the model, the calculation of cumulative infiltration is performed iteratively as given in Eq. (6.2); afterward, the infiltration rate is calculated using Eq. (6.3). Equations (6.2) and (6.3) are described as follows:

$$F(t) = Kt + (h_0 - \psi)\Delta\theta \ln\left(1 + \frac{F(t)}{(h_0 - \psi)\Delta\theta}\right) \quad (6.2)$$

$$f(t) = K\left(1 + \frac{(h_0 - \psi)\Delta\theta}{F(t)}\right) = \frac{dF}{dt} \quad (6.3)$$

where  $F(t)$  denotes the cumulative depth of infiltration;  $f(t)$  describes the infiltration rate in terms of the temporal change in the cumulative infiltration depth;  $K$  denotes the hydraulic conductivity at the residual air saturation, which is assumed to be 50% of the saturated hydraulic conductivity,  $K_s$  (Whisler and Bouwer 1970). The capillary suction head at the wetted front of the soil is given with  $\psi$ ,  $h_0$  is the ponding water depth, and  $\Delta\theta$  is the increase in moisture content calculated by the difference between the effective porosity,  $n$ , and the initial moisture content,  $\theta_i$ . The effective porosity, capillary suction head at the wetted front, and hydraulic conductivity are the so-called Green-Ampt parameters, which can be estimated from the given soil

texture class. There exist different approaches to account for such a crust; a simple approach can be seen in Brakensiek and Rawls (1983), in which the effective hydraulic conductivity of the crust and subcrust soil is calculated by a harmonic mean (Rawls et al. 1990). Table 6.1 shows the Green-Ampt parameters for four different soil texture classes described by Rawls et al. (1983).

Other values of the parameters are given in the user manuals of the hydraulic and hydrologic modeling software XPS storm and XPSWMM of the Innovyze company (2019) based on different sources. These manuals state that higher initial soil moisture deficit values are applicable for very dry conditions, and lower values should be used when wetter initial conditions occur. The values for four different soil texture classes are given in Table 6.2.

Comparing the values from Innovyze (2019) with those from Rawls et al. (1983) shows that the hydraulic conductivity for sand from Rawls et al. (1983) is approximately one order of magnitude higher than the maximum value from Akan (1993), and the value for loamy sand is more than double the one from Akan, while the values are similar for sandy clay loam from Rawls et al. (1983) and for clay loam from Akan (1993). For clay, the value from Rawls et al. (1983) is closer to the minimum value than to the maximum value from Akan (1993). The average capillary suction head values from Rawls et al. (1983) are lower than those from Innovyze (2019) for all soil types except clay, for which the value from Rawls et al. (1983) is almost double that from Innovyze (2019).

If it is expected that the considered soil will generate a surface crust with a lower hydraulic conductivity than the subcrust soil, a modified infiltration model can be used to account for such a crust. There exist different approaches to designing this mode; a simple approach can be seen in Brakensiek and Rawls (1983), in which the effective hydraulic conductivity of the crust and subcrust soil is calculated by a harmonic mean (Rawls et al. 1990):

$$K_e = \begin{cases} K_c & \text{for } Z_f \leq Z_c \\ \frac{Z_f}{\frac{Z_f - Z_c}{K} + \frac{Z_c}{K_c}} & \text{for } Z_f > Z_c \end{cases} \quad (6.4)$$

where  $K_e$  is the effective hydraulic conductivity,  $K_c$  is the hydraulic conductivity of the crust,  $Z_c$  is the crust thickness, and  $Z_f$  denotes the wetted depth, which is

**Table 6.1** Average Green-Ampt parameters

Soil texture class	Effective porosity $n$ (-)	Capillary suction head $\psi$ (cm)	Hydraulic conductivity $K$ (cm/h)
Sand	0.417	4.95	11.78
Loamy sand	0.401	6.13	2.99
Sandy clay loam	0.330	21.85	0.15
Clay	0.385	31.63	0.03

Source Rawls et al. 1983

**Table 6.2** Typical values of Green-Ampt parameters given in the user manuals of XPStorm and XPSWMM

Parameter	Typical initial moisture deficit at wilting point ( $m^3/m^3$ )	$\psi$ (cm)	$K$ (cm/h)
Reference	(Clapp and Hornberger 1978)	Several; sources not given	(Akan 1993)
Sand	0.34	10.16	0.76–1.14
Loamy sand	–	–	0.76–1.14
Clay loam	0.24	25.40	0.00–0.13
Clay	0.21	17.78	0.00–0.13

Source Innovyze (2019)

calculated by dividing the cumulative infiltration depth from the previous timestep by the soil moisture deficit.

### 6.2.3 Study Area

El Gouna is a tourist town 25 km north of Hurghada in the Red Sea Governorate of Egypt. It is located inside the catchment of Wadi Bili. The total catchment area of Wadi Bili is approximately 880 km<sup>2</sup>, and the wadi flows from the Red Sea Mountains, passes through a narrow channel to the coastal plain of El Gouna and finally drains into the Red Sea. In recent years, the region of El Gouna has been affected by flash floods several times, leading to road and infrastructure damage. Measurements of the rainfall and runoff of the event that occurred on March 09, 2014 were carried out and published in Hadidi (2016). Figure 6.1 shows the location of Hurghada in Egypt (a) and the topography and catchment area of Wadi Bili (b). Panel 1(c) represents the region of El Gouna on the coastal plain, including the location of the discharge measurements collected in 2014 in a narrow valley upstream of where the wadi spreads into a wider delta.

### 6.2.4 Data for Validation of Results

As it is usually difficult to obtain direct measurements of flash flood events, alternative data sources need be considered to enable a validation of the results. In this study, three different kinds of data are taken into account: multispectral satellite images, pictures taken by the community, and statements from the community.

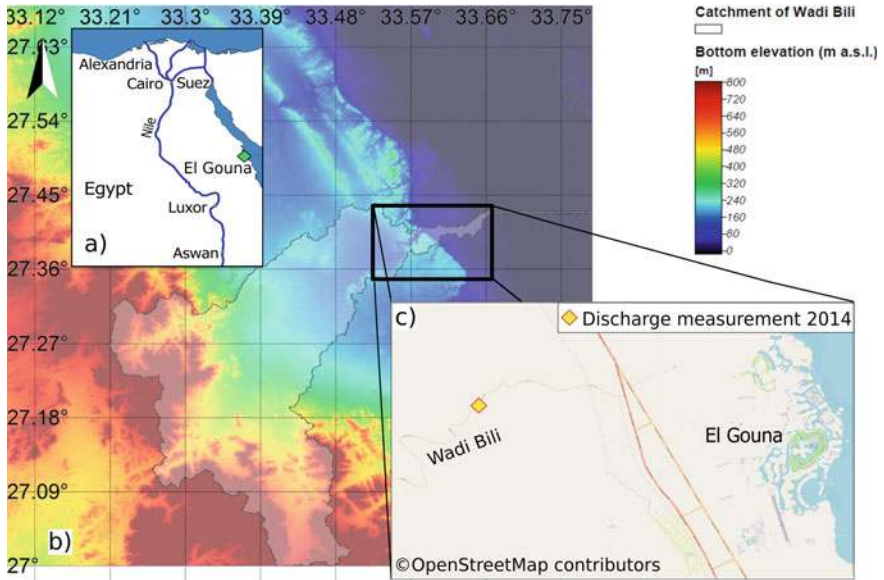


**Fig. 6.1** a) location of Hurghada in Egypt (made with Natural Earth), b) topography and Wadi Bili catchment (delineated from SRTM DEM and visualized with SAGA GIS), and c) location of discharge measurements from Hadidi (2016) and the city of El Gouna (map: ©OpenStreetMap contributors)

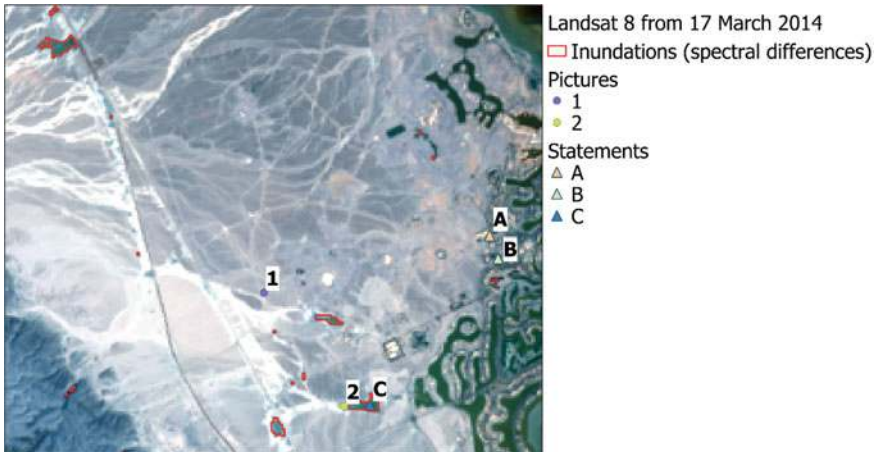


**Fig. 6.2** Landsat 8 image from 17 March 2014 indicating the locations of the pictures and statements as well as the inundated areas obtained from automatically detection of land use changes from the spectral distance between Landsat 8 images of 20 February and 17 March 2014 (Landsat 8 image courtesy of the U.S. Geological Survey)



Figure 6.2 shows the locations at which information of these three different sources was obtained; the information types are further described in the next sections.

#### 6.2.4.1 Landsat 8 Images

Images from the Landsat 8 satellite, which was launched in February 2013, are available for the time of the considered flash flood event in El Gouna in March 2014. These images contain eleven different bands with different resolutions; most of them have a resolution of 30 m. The “Semi-Automatic Classification Plugin” (SCP) was used to download the images directly in QGIS (Congedo 2016). As the temporal resolution of 16 days is relatively coarse and, due to excessively high cloud cover during the days of the rainfall event itself, the images of 20 February and March 17, 2014 were chosen as the best images to be compared to detect the inundated areas caused by the event on 9 March 2014. Both images are shown in Fig. 6.3, and when the images are compared, it becomes obvious which areas were still inundated 8 days after the event. Following the SCP documentation, only bands 2–7 were considered, and the band processing tool “Spectral distance” was used to automatically detect land cover changes between 20 February and March 17, 2014. “Spectral angle mapping” was chosen as the distance algorithm, and the distance threshold was set to 10. After vectorizing the results and extracting them for the land surfaces, the polygons of inundated areas observed from the Landsat 8 images are shown with red polygons in Fig. 6.2.

#### 6.2.4.2 Pictures

Another important source of information about the inundated areas and estimated water depths that occurred during the event are pictures that were taken during and



**Fig. 6.3** Landsat 8 images from 20 February 2014 (left) and March 17, 2014 (right) (Landsat 8 image courtesy of the U.S. Geological Survey)

after the event. In this study, it was very important to obtain the geographical information on the location where each picture was taken. The best case occurs when the geotag function was activated on the used device while taking the pictures. Another possibility is to locate each picture as precisely as possible by descriptions or through orientation based on striking features in the surroundings. Many pictures were collected from the flash flood event in March 2014, but unfortunately, only very few of them were geotagged. Two of these photos were chosen and are shown in Fig. 6.4. The left panel shows an inundated road with a driving car. The water depth can be estimated to be between 10 and 25 cm, as the car tire seems to be inundated up to less than half of its diameter. The right picture shows an inundated area with some children. The water depth can be estimated to be approximately 25–35 cm as the water goes up to the knees of the children. The locations obtained from the geotags are indicated with circles in Fig. 6.2; 1 indicates the location of the left picture, and 2 indicates the location of the right picture.

### 6.2.4.3 Statements

The third source of information used in this study are statements from persons who were in El Gouna at the time of the event and observed the inundations in different areas. To gather these statements, requests for information on and pictures of the events were shared in different groups on Facebook and via email. Furthermore, a



**Fig. 6.4** Pictures of inundated areas were taken on March 09, 2014, at 15:04 (Picture 1, left) and on March 10, 2014, at 12:49 (Picture 2 right). The right picture was modified for reasons of data protection to make the shown persons unrecognizable. *Source* private

questionnaire was created with KoboToolbox, in which the locations of observed inundations can be directly tagged within the toolbox and pictures can be uploaded.

### 6.3 Model Setup

To simulate the flood extent, water depths, and flow velocities for the region of El Gouna, a shallow-water model was set up for a domain of approximately 9 km × 11 km. The grid consisted of 438,372 rectangular cells of 15 m × 15 m each. To consider the topography of the model area, the digital surface model (DSM) ALOS WORLD 3D (JAXA 2017) was used, as it was concluded in preliminary studies that this model represents the study area better than other freely available digital surface models with the same resolution, 30 m, namely, SRTM, and ASTER GDEM2 (Tügel et al. 2018). To reach smoother gradients between the cells, inverse distance weighted interpolation with an output cell size of 10 m was conducted by using QGIS. As most of the buildings were not included in the original DSM, buildings were incorporated from open street map polygons by increasing the elevation of the original DSM by 10 m. Figure 6.5 shows the interpolated DSM, including buildings, for the model domain. A Manning coefficient of  $0.01 \text{ m}^{-1/3} \cdot \text{s}$  was used to represent the friction of bare sand based on the values given in Engman (1986). As an initial condition, the system was considered to be completely dry. The incoming flood wave from the Wadi Bili catchment was taken into account with a boundary condition at the channel cross-section, where Hadidi (2016) carried out flow velocity measurements and estimated the water depths and runoff rates during the event on March 09, 2014. The inflow hydrograph considered in this study, which has a peak discharge of  $47.5 \text{ m}^3/\text{s}$ , was generated from a hydrological model presented in Tügel et al. (2020b) that was calibrated with the hydrograph observed by Hadidi (2016). The temporal distribution of rainfall with a resolution of 10 min that was recorded during the event in 2014 at the weather station at TU Berlin Campus El Gouna was considered a source term for all cells inside the model domain. A total time period of 45 h was simulated to calculate the flow propagation inside the domain.

## 6.4 Results and Discussion

### 6.4.1 Simulated Flow Field Without Infiltration

The simulation results include the flood extents, spatial distributions of water depths, and flow velocities every three hours over the total simulation time of 45 h. These outputs enable an analysis of the temporal and spatial developments of the flood event. Figure 6.6 represents the simulated flow velocities, and Fig. 6.7 shows

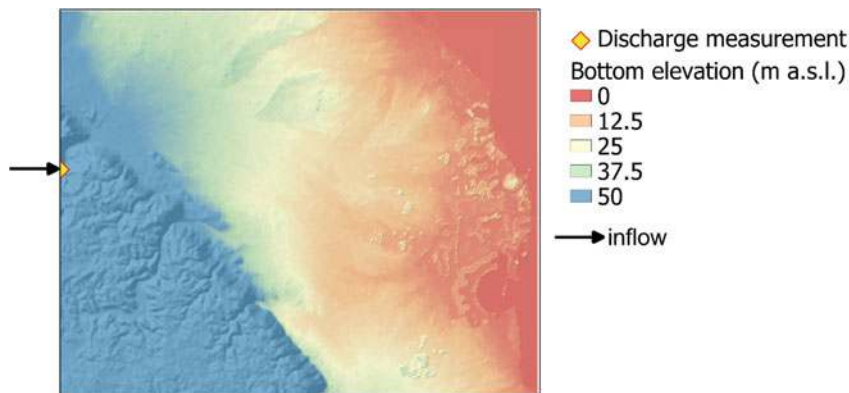


**Fig. 6.5** Model domain, location of inflow, and topography from the AW3D digital surface model and incorporated buildings from Openstreetmap polygons

the simulated water depths after 9 h, when the maximum water depths were simulated, in a zoomed-in part of the model domain with open street maps in the background to better locate the inundated areas within the city. The analytical hillshade in the background allows the visualization of elevation and improves the visibility of buildings, which were incorporated in the DSM. The flood came from Wadi Bili at the western boundary of the domain and spread into different flow paths, some of which propagated to the northeastern direction, crossing the model boundaries, and continued beyond the considered domain. Other flow paths propagated to the southeast direction to the city of El Gouna. In addition to the incoming flood wave from the wadi catchment, the rainfall inside the domain also generated streams at different locations, and water accumulated in several depressions. The area around the campus of TU Berlin (denoted by A in Fig. 6.6 and Fig. 6.7) and the area around the student dorms (denoted by B in Fig. 6.6 and Fig. 6.7) were only affected by rainfall inside the domain, and water depths up to 0.20 m were simulated, which agrees well with the statements given for these locations (see Table 6.3); although the time in the first statement was 7 pm, and the timestep shown in the figure is 9 pm. However, the timestep for 6 pm also showed inundations of approximately 0.10 m, which agrees well with the statement that the shoes of individuals were submerged. In the northwest corner of the depicted section, a large flooded area was observed in the Landsat 8 images, where inundations with water depths of approximately 0.20 m were also simulated. At all locations where inundations were observed and reported by at least one of the considered sources, a flooded area with a certain water depth was simulated. Only at location 1 was no water depth simulated although flooded roads were observed at this location, as shown in Picture 1 (Fig. 6.4, left). In the close surroundings of that location, water depths up to 0.50 m were simulated. Additionally, it must be taken into account that the geotags of the pictures might not be very accurate. At location C, where maximum inundations of 2.00 m were reported within the questionnaire,

the maximum simulated water depth was only 0.40 m. On the other hand, Picture 2 (Fig. 6.4, right), which is close to location C, led to an estimated water depth of approximately 0.25–0.35 m, which fits quite well with the simulated water depths. A large flooded area with an overall maximum water depth of approximately 1 m was simulated close to the desalination plant (indicated with a red X in Fig. 6.7), while none of the considered observation sources indicated specifically high water depths at this location. From earlier personal exchanges with staff members of the desalination plant, it is known that inundations were also observed there but not in the range of 1 m. Flow velocities between 0.5 and 2.5 m/s were simulated for most streams. These numbers seem to be reasonable, as during a smaller flash flood event in the same area that occurred on October 27, 2016, flow velocities of approximately 1 m/s were measured by one coauthor in a stream next to the main connection road, which crosses the section shown in Figs. 6.6 and 6.7 from the north-northwest to the south-southeast.

### 6.4.2 Infiltration

As most parts of the model domain consist of natural bare surfaces and mostly sandy soils with high hydraulic conductivities, infiltration should not be neglected. In this section, the obtained results when accounting for infiltration with the Green-Ampt model are represented for different parameter values. Taking into account the average Green-Ampt parameters for loamy sand from Rawls et al. (1983) (see Table 6.1) and an initial moisture content of  $0.03 \text{ m}^3/\text{m}^3$ , assuming very dry soil before the rainfall event, all the water infiltrated before reaching the city of El Gouna (Fig. 6.8 left). Taking into account the parameter values for sand from Innovyze

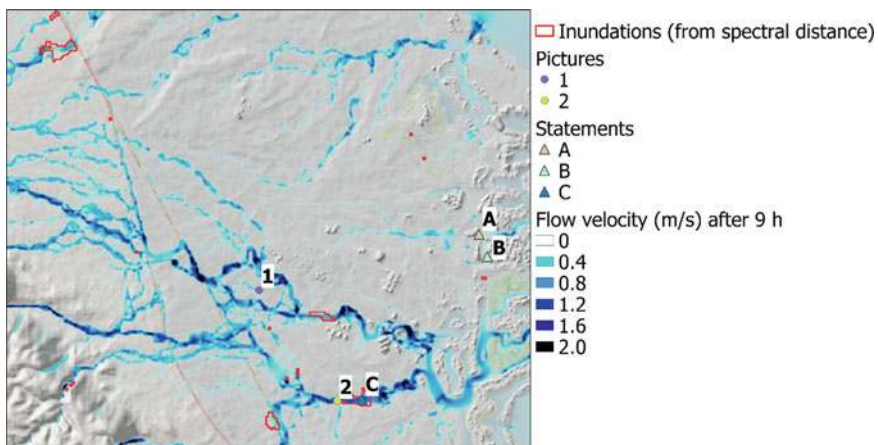


**Fig. 6.6** Simulated flow velocities after 9 h of simulated time, including the locations of observations as described in Sect. 6.2.4

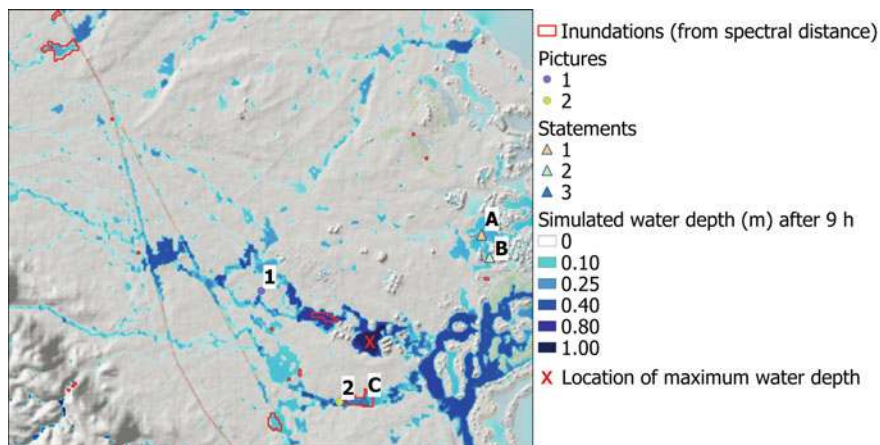


**Fig. 6.7** Simulated water depths after 9 h of simulated time, including the locations of observations as described in Sect. 6.2.4

**Table 6.3** Statements from the El Gouna community regarding inundated areas and water depths during the flash flood event in El Gouna on March 09, 2014

Location	Statement	Source
A	<i>The flood kind of receded in about a day. After that, the road was quite bad and slippery We stayed the night in the uni, as we could not move out at all</i>	Facebook group for students of TU Berlin Campus El Gouna
Between A and B	<i>I remember that the area between the university and the dorms was flooded (dorms: location B)</i>	Facebook group for students of TU Berlin Campus El Gouna
Between A and B	<i>By around 7 pm, I remember our shoes were submerged ankle deep in front of the library building</i>	Facebook group for students of TU Berlin Campus El Gouna
Between A and B	<i>The ground where GSpace is currently situated, water stagnation had happened for days</i>	Facebook group for students of TU Berlin Campus El Gouna
C	<i>Maximum observed water depth of estimated 2 m near El Gouna cable park</i>	Questionnaire created with KoboToolbox

(2019) (see Table 6.2), the flood wave propagated slightly further than in the case of loamy sand from Rawls et al. (1983), but most of the area around El Gouna was still completely dry - the local rainfall did not lead to any surface runoff as it directly infiltrated, and most of the locations where inundations were reported from the considered sources (see Sect. 6.2.4) did not show any water depths. Therefore, it can be concluded that both sets of Green-Ampt parameters for sandy soil strongly overestimate infiltration.

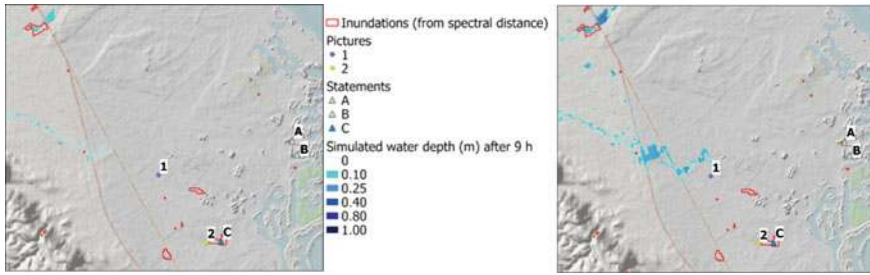


**Fig. 6.8** Water depths after 9 h of simulated time for the average Green-Ampt parameter values for loamy sand from Rawls et al. (1983) (left) and for sand from Innovyze (2019) with the minimum hydraulic conductivity value (right)

Figure 6.9 shows the water depths after 9 h as simulated for sandy clay loam from Rawls et al. (1983) and for sand from Rawls et al. (1983), as well as for sand from Innovyze (2019), both accounting for a surface crust (after Eq. 6.4) of 5 mm thickness and a hydraulic conductivity equal to that for clay from Rawls et al. (1983) (see Table 6.1). All three of the simulations show very similar distributions of flooded areas, with some differences in water depths. The simulated flooded areas were still significantly reduced compared to the case without infiltration (Fig. 6.7), but surface runoff also occurred in the city area, leading to inundations in some areas. At most locations where inundations were reported via at least one of the considered sources (see Sect. 6.2.4), significant water depths were simulated. However, at locations, A and B corresponding to the statements that report inundations around Campus El Gouna and the student dorms, only small water depths with a maximum of 0.05 m were simulated. In most parts of the study area, the dominant soil type is sand with pebbles, sometimes combined with mud (Hadidi 2016), but only the parameters for finer soil texture classes, such as sandy clay loam, or the consideration of a surface crust with a reduced hydraulic conductivity led to surface runoff in some areas of El Gouna as it was observed during the event in 2014.

To further investigate the suitability of these three infiltration settings, the temporal development of the water depths inside three of the major ponds that were observed by the Landsat 8 image taken on 17 March are plotted in Fig. 6.10, and the location of each pond is labeled in Fig. 6.9 with P1, P2, and P3. In addition to the results of the three infiltration settings, the water depths that were simulated if no infiltration was considered are shown in Fig. 6.10. It can be seen that at all three locations, the water depth dropped to zero at first for the case of sand from Rawls et al. (1983) with a crust, second for the case of sand from Innovyze (2019) with a crust, and then for sandy clay loam from Rawls et al. (1983). As the crust effect regarding decreased hydraulic conductivity decreases with ongoing time and increasing wetted depth (see Eq. (6.4)), considering the case of sand from Rawls et al. (1983) with a crust again resulted in overestimating infiltration after a certain time. The same effect is valid for the case of sand from Innovyze (2019), but due to

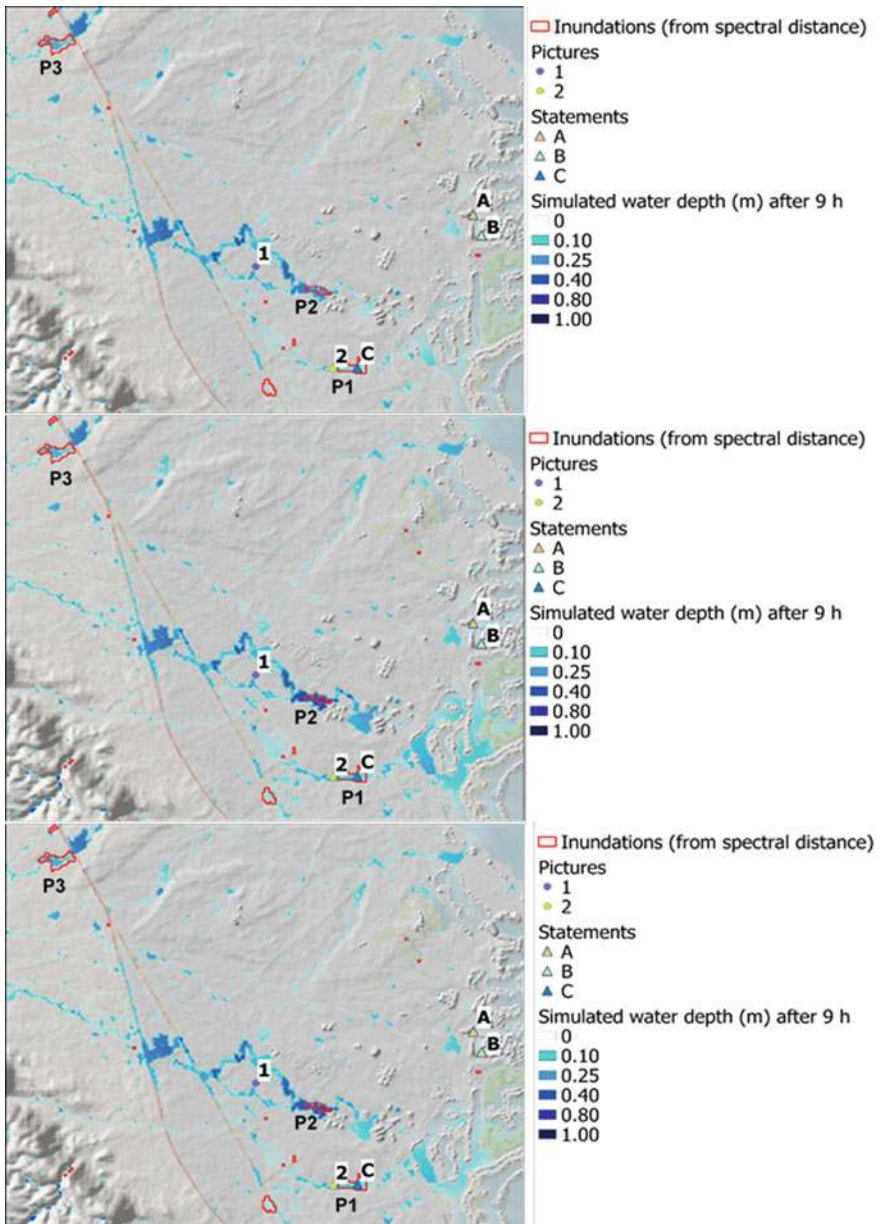


**Fig. 6.9** Spatial distributions of water depth after 9 h for the cases of sandy clay loam from Rawls et al. (1983) (top), sand from Rawls et al. (1983) with a surface crust (middle), and sand from Innovyze (2019) with a surface crust (bottom)



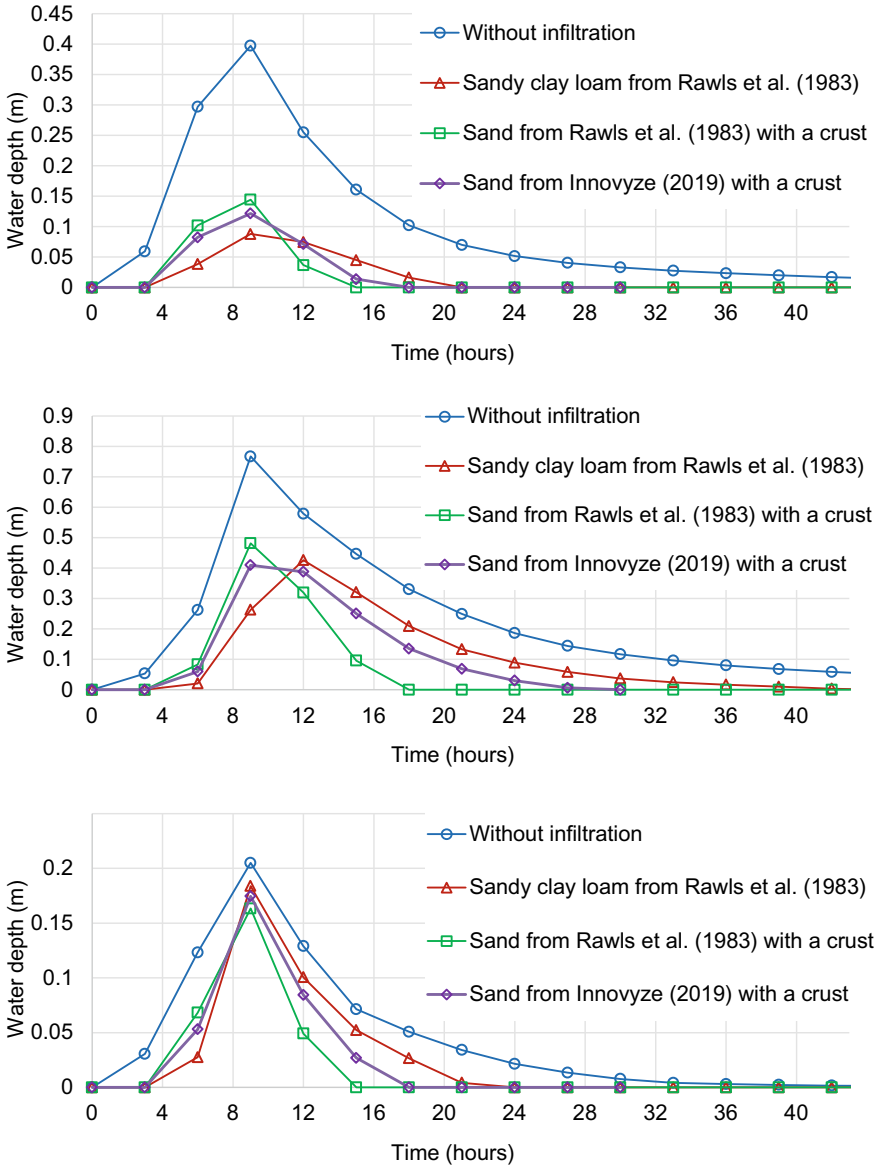


**Fig. 6.10** Temporal development of water depths inside pond P1 (top), pond P2 (middle), and pond P3 (bottom); the locations of the ponds are indicated in Fig. 6.9. The temporal resolution is three hours

the smaller hydraulic conductivity of the subcrust sand compared to the values from Rawls et al. (1983) the overestimation of the infiltration is smaller, but the water also completely disappeared after approximately 18 h (P1 and P3) and 28 h (P2).

The results of the case considering sandy clay loam from Rawls et al. (1983) seem to be more reasonable than the two other cases, but in this case, the water still disappeared at all three locations after approximately 21 h (P1), 41 h (P2), and 28 h (P3). The flow velocities for these three infiltration settings were reduced in many areas compared to those simulated in the case without infiltration but still lie between 0.5 and 2.5 m/s in the main streams.

For the case without infiltration, there was still some water present at the locations of the observed ponds P1 and P2, but only in the range of 0.02 m in depth at P1 and 0.05 cm in depth at P2, while at P3, the water disappeared by the end of the simulation time of 45 h. As the ponds were still quite large on March 17, 2014 (eight days after the event), it can be concluded that even the simulation without infiltration seemed to underestimate the water depth at those locations. When looking at the Landsat 8 images of later dates, it becomes obvious that P2 disappeared approximately one month, P1 between one and two months, and P3 approximately five months after the rainfall event. Therefore, in addition to the overestimation of infiltration, an incorrect representation of the topography of the area is most likely another reason for the underestimated water depth obtained in the simulations, as there might be deeper depressions or blockages of the flow paths causing higher water depths and larger flooding areas that are not well-captured in the relatively coarse DSM. The next section further investigates the digital surface model (DSM) and introduces modifications in certain areas based on observations from satellite data as well as from pictures of the area.

### 6.4.3 Correction of DSM

As shown in the previous section, some characteristics are not well-captured in the DSM, leading to underestimations of water depths; for example, the water depths were underestimated at the locations of several ponds that were observed by Landsat 8 images. If a high-resolution and accurate DSM is not available for a certain study area, the best option would be to carry out field surveys and create a high-resolution DSM, e.g., one derived from laser-scanning data recorded with the help of an unmanned aerial vehicle (UAV). As the necessary capacities for such investigations are not available, the given DSM can also be modified based on observations in the field, from satellite images, or from pictures of the area. Three major modifications were carried out to the DSM of the model domain with regard to the three observed ponds, P1, P2, and P3: (1) the elevation of the main road that crosses the model domain from north-northwest to south-southeast was increased; (2) the wall around Scarab Club El Gouna was incorporated; (3) the dam directly east of pond P1 was incorporated, as observed from satellite images taken in February 2014. The locations of these modifications are presented in Fig. 6.11, and the reasons and explanations for each of the three modifications are given in the following sentences. In Fig. 6.12 (top), the water depths after 45 h are represented when taking into account the original DSM (without infiltration), showing a large pond in the upper-left corner

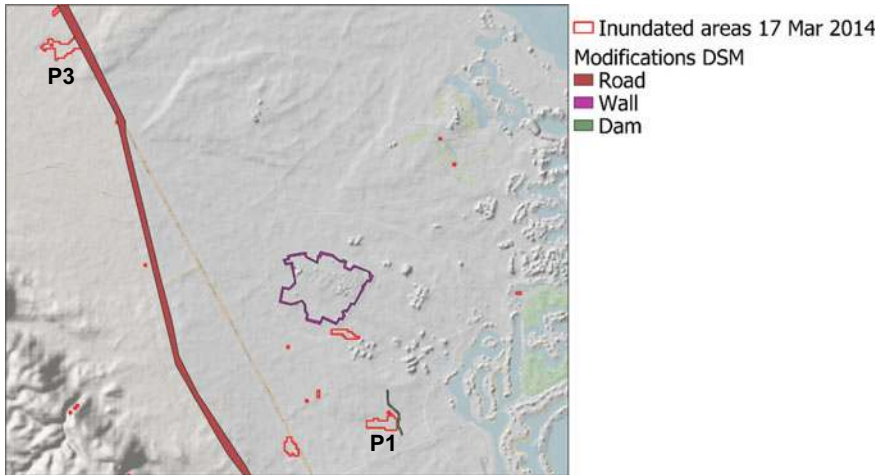


**Fig. 6.11** Locations of carried out modifications in the DSM

of the depicted section. In the simulation results, this pond is located east of the road, while pond P3 is located directly on the other side of the road, as observed in the Landsat 8 images. This leads to the conclusion that the road is probably blocking the flow path, resulting in an accumulation of water west of the road instead of east of the road. From pictures taken of the area, it can be seen that the road is slightly elevated and has a high curbstone, while the original DSM shows a small lowering of the road compared to the adjacent area. To better capture the blocking of the flow path through the elevated road, the area of the road was elevated by 0.50 m in the DSM. The second modification incorporated a wall around the Scarab Club El Gouna, which is located north of P2. This wall was not included in the original DSM and might lead to redirections of flows in the corresponding area. The elevation in the area of the wall was increased by 10 m. The third modification was performed east of pond P1, as seen in satellite images from the time before the event in March 2014, when a sand dam was built to block the flow at that location. To include the dam in the DSM, the elevation at the location of the dam was elevated by 1 m. Figure 6.12 (middle) shows the water depths after 45 h taking into account the modified DSM without infiltration, and Fig. 6.12 (bottom) shows the water depths with infiltration considering sandy clay loam from Rawls et al. (1983). For both cases, ponds P1 and P3 are much better captured than in Fig. 6.12 (top), where the original DSM was taken into account, while P2 is slightly better represented with the modified DSM when no infiltration is considered but is not well-captured if infiltration with sandy clay loam is taken into account.

Figure 6.13 shows the temporal development of the water depths at P1, P2, and P3 considering the modified DSM without infiltration (top) and with infiltration through sandy clay loam (bottom). While the water depth considerably increased at P1 and P3 after the modification of the DSM, it remained almost the same at P2

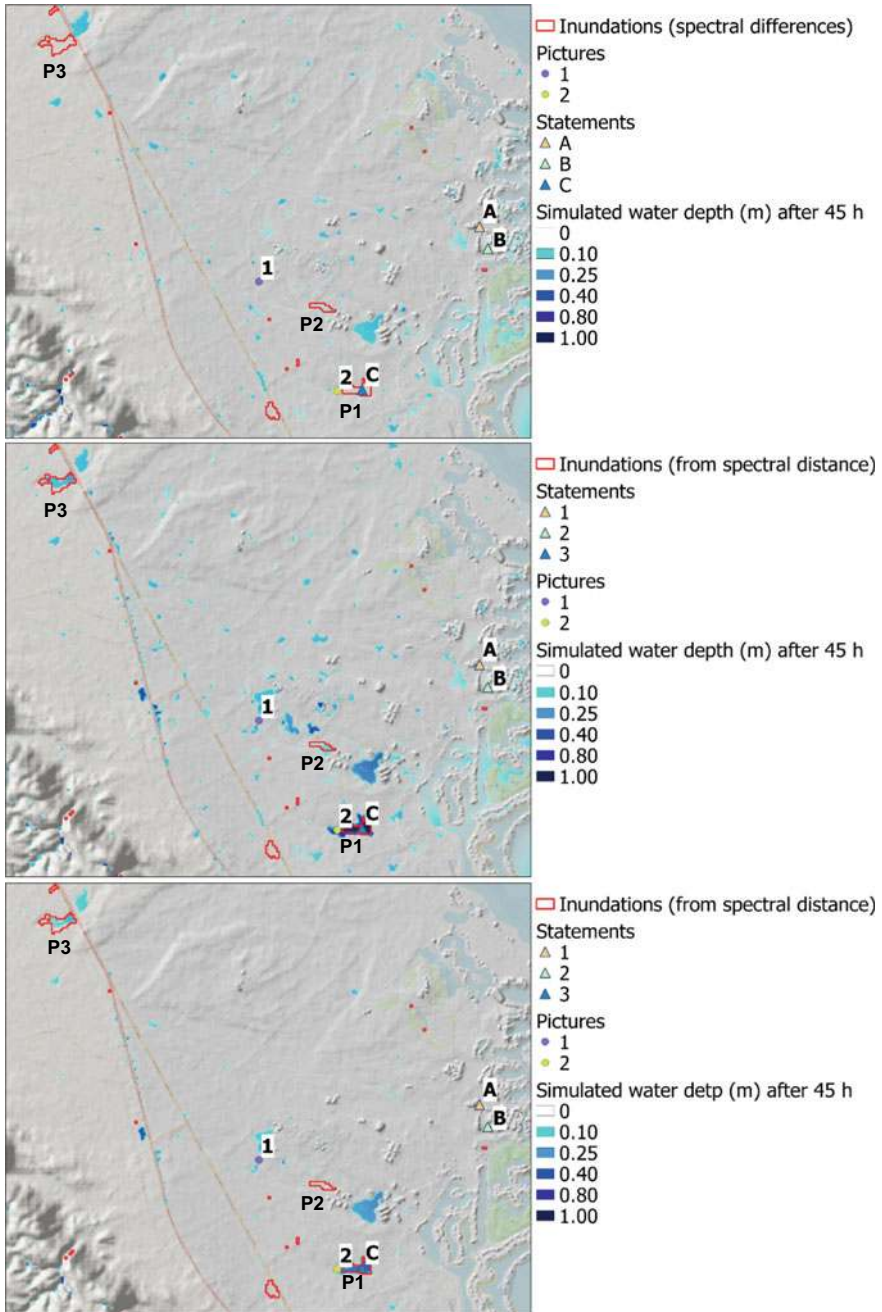


**Fig. 6.12** Spatial distributions of water depths after 45 h of simulated time considering the original DSM without infiltration (top), the modified DSM without infiltration (middle), and the modified DSM accounting for infiltration with the Green-Ampt parameters for sandy clay loam from Rawls et al. (1983)

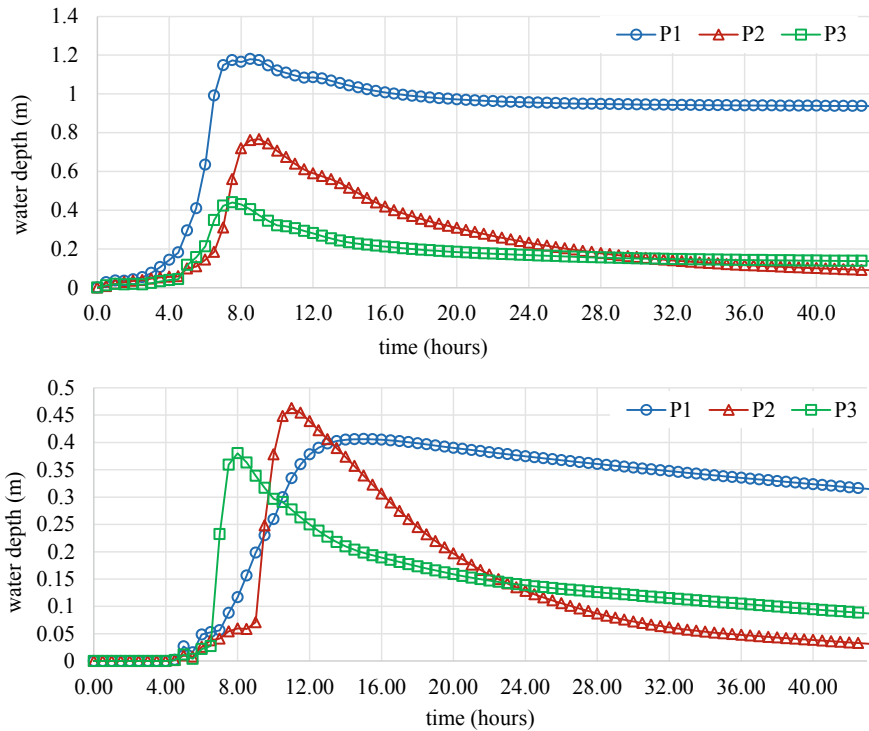


**Fig. 6.13** Temporal development of the water depths of ponds P1, P2, and P3 considering the modified DSM without infiltration (top) and the modified DSM with infiltration through sandy clay loam from Rawls et al. (1983); the locations of ponds are indicated in Fig. 6.12; the temporal resolution is 30 min

compared to the water depth calculated with the original DSM, shown in Fig. 6.10. Therefore, the wall around the Scarab Club El Gouna north of P2 had only a very small influence on the water depth at P2. There might be additional features in the area of P2 that are not represented appropriately in the DSM, leading to higher observed water depths than the simulated ones.

Of course, all presented modifications in the DSM are based on strongly simplified assumptions and rough estimations of the modified elevations. Furthermore, there might be further features that are not captured appropriately in the DSM, such as a fourth pond located west of P1 that is also not well-captured in the simulation results as well as inundated areas indicated in statements A and B. In general, the results underline the importance of accurate and high-resolution topographical data, which is unfortunately often not available or not easily accessible. However, as the results could be clearly improved with regard to the observed ponds P1 and P3, it can also be concluded that a careful modification of the DSM to incorporate known features can significantly improve the simulation results. Of course, only available observations, e.g. from satellite images or photographs, can justify these modifications as long as there are no accurate data from topographical surveys available.

## 6.5 Conclusions

In this study, the flash flood event that occurred on 9 March 2014 in the region of El Gouna, Egypt, was simulated with a robust 2D shallow-water model using the hydroinformatics modeling system (hms), and the results were validated with observations from different sources. As direct measurements of water depths and flow velocities are often not available for flash floods, especially in data-scarce regions such as the region where the study area is located, alternative sources must be taken into account. Here, multispectral images from the Landsat 8 satellite, pictures of inundations taken from the community in El Gouna, and statements from persons who observed the flooded areas during and after the event were collected to compare the simulation results with these observations.

The results after nine hours of simulated time agreed relatively well with most of the observed flooded areas and were plausible in terms of the ranges of water depths and flood extents, while there were a few locations where the model underestimated the observed flood extents and water depths. The simulated flow velocities seem to be plausible compared to the velocities measured during a smaller flash flood event in the same area. As the investigated area consists mostly of bare sand, infiltration should not be neglected and was taken into account with the time-dependent Green-Ampt model. When the Green-Ampt parameters were set to values indicated in two different sources in the literature for the dominant soil types of sand and loamy sand, infiltration was strongly overestimated by the model, while the consideration of a surface crust with a thickness of 5 mm and the hydraulic conductivity of clay or the consideration of the literature-obtained values for sandy clay loam instead of sand led to much better agreements of the simulation results with the observations. For locations where inundations were observed even a few days up to a few months after the rainfall event, most of the water had already drained out of the area by the end of the simulation time of 45 h, even if no infiltration was considered in the model. This led to the conclusion that in addition to the overestimation of infiltration, the DSM lacked accuracy and resolution, so some important topographical features that had significant impacts on the flow paths and the development of flooded areas were not well captured. Three modifications in the DSM were introduced based on observations from satellite images and personal photographs, and the simulation results of the modified DSM agreed much better with the observed flood extents and water depths at the end of the simulation time of 45 h. Nevertheless, the DSM most likely still lacked other important features, so the flood extent and water depth were still underestimated at several locations. Although the DSM needs further improvements, the model results, such as the maps of flooded areas, support the risk assessment, and different structural mitigation measures can be incorporated in the model to investigate their effectiveness for different rainfall events.

Overall, it could be shown that the considered data sources in terms of satellite images and community-based pictures and statements can be used for a rough validation of the model results if no direct measurements are available. A drawback

of using Landsat-8 images is its relatively low temporal resolution, which makes it difficult to examine the extent of floods immediately after rainfall events. Therefore, only flooded areas that remained for a longer time can be observed from these satellite images. Data from the Sentinel-2 satellites that were launched in June 2015 (2A) and March 2017 (2B) have higher temporal resolutions of approximately 5 days and spatial resolutions of 10 m, which makes these data even more suitable for analyzing events that occurred more recently.

Due to the rather low temporal resolution of satellite images and because it remains challenging to estimate water depths from satellite images, community-based information in terms of statements and pictures is also very important for assessing model results if no direct measurements are available. Although the event occurred several years ago at the time the requests were sent to the community, several useful statements were collected. Regarding the collected pictures, the problem was not the number of photos but rather the localizations of their recordings, as most of the photos were not geotagged. Currently, as the usage of smartphones with very good cameras and often automatically activated geotagging has considerably increased in recent years, it is probably much easier to find pictures that include corresponding geospatial information. As the general activity on different social media platforms is also continuously increasing, it is likely that many more pictures and statements from social media communities could be found for more recent flood events, especially with the help of machine learning techniques.

The next steps are to conduct infiltration measurements with a rainfall simulator to better represent the natural conditions during heavy rainfall events and to investigate the effect of surface sealing. These steps will enable more appropriate implementations of infiltration processes in the model. In general, a further improvement of the DSM is needed to achieve more accurate results.

**Acknowledgments** This work was supported by TU Berlin, Germany. The travel grants of the DFG Research Training Group “Urban Water Interfaces” (GRK 2032/1) are gratefully acknowledged. The simulations were computed on the supercomputers of Norddeutscher Verbund für Hoch—und Höchstleistungsrechnen in Berlin and Göttingen as well as on the HPC cluster of TU Berlin.

## References

- Akan AO (1993) Urban stormwater hydrology: a guide to engineering calculations. Technomic Pub. Co, Lancaster, Pa
- Brakensiek D, Rawls W (1983) Agricultural management effects on soil water processes. Part II: green and Ampt parameters for crusting soils., pp 1753–1757. *Trans ASAE* 26(6):1753–1757
- Busse T, Simons F, Mieth S, Hinkelmann R, Molkenthin F (2012) HMS: a generalised software design to enhance the modelling of geospatial referenced flow and transport phenomena. In: Proceedings of the 10th international conference on hydroinformatics—HIC 2012, Hamburg
- Clapp RB, Hornberger GM (1978) Empirical equations for some soil hydraulic properties. *Water Resour Res* 14(4):601–604

- Congedo L (2016) Semi-automatic classification plugin documentation
- Engman E (1986) Roughness coefficients for routing surface runoff. *J Irrig Drain Eng* 11(1):39–53
- Esteves M, Faucher X, Galle S, Vauclin M (2000) Overland flow and infiltration modelling for small plots during unsteady rain: numerical results versus observed values. *J Hydrol* 228(3–4):265–282
- Fernández-Pato J, Caviedes-Voullième D, García-Navarro P (2016) Rainfall/runoff simulation with 2D full shallow water equations: sensitivity analysis and calibration of infiltration parameters. *J Hydrol* 536:496–513
- Ghazal A (2018) Urban flood protection in arid regions King Fahd suburb in Dammam—Saudi Arabia. Master's thesis, TU Berlin Campus El Gouna, Water Engineering
- Green W, Ampt G (1911) Studies on soil physics, Part I, the flow of air and water through soils. *J Agric Sci* 4:11–24
- Hadidi, A (2016) Wadi Bili catchment in the Eastern Desert—flash floods, Geological model and hydrogeology. Dissertation. Fakultät VI—Planen Bauen Umwelt der Technischen Universität Berlin, Berlin
- Hou J, Liang Q, Simons F, Hinkelmann R (2013) A stable 2D unstructured shallow flow model for simulations of wetting and drying over rough terrains. *Comput Fluids* 132–147
- Hou J, Zhang Y, Tong Y, Guo K, Qi W, Hinkelmann R (2019) Experimental study for effects of terrain features and rainfall intensity on infiltration rate of modelled permeable pavement. *J Environ Manage* 177–186
- Hou J, Wang N, Guo K, Li D, Jing H, Wang T, Hinkelmann R (2020) Effects of the temporal resolution of storm data on numerical simulations of urban flood inundation. *J Hydrol* 125100
- Innovyze (2019) Help documentation of XPSWMM and XPStorm. Available <https://help.innovyze.com/display/xps/Infiltration> Accessed 30 April 2020
- JAXA (2017) ALOS global digital surface model “ALOS World 3D—30 m (AW3D30)”. Available <http://www.eorc.jaxa.jp/ALOS/en/aw3d30/index.htm>. Accessed 20 Feb 2017
- Liang Q, Xing Y, Ming X, Xia X, Chen H, Tong X, Wang G (2017) An open-source modelling and data system for near real-time flood forecasting. In: E-proceedings of the 37th IAHR World Congress, 13–18 Aug, 2017, Kuala Lumpur, Malaysia
- Morin J, Benyamini Y (1977) Rainfall infiltration into bare soils. *Water Resour Res* 13(5): 813–817
- Müller E (2007) Scaling approaches to the modelling of water, sediment and nutrient fluxes within semi-arid landscapes. Jornada Basin, New Mexico. Logos Verlag Berlin. PhD thesis submitted 2004 to King's College London, UK
- Murillo J, García-Navarro P, Burguete J (2009) Conservative numerical simulation of multi-component transport in two-dimensional unsteady shallow water flow. *J Comput Phys* 15:5539–5573
- Nciizah A, Wakindiki I (2015) Soil sealing and crusting effects on infiltration rate: a critical review of shortfalls in prediction models and solutions. *Arch Agron Soil Sci* 61(9):1211–1230
- Ni Y, Cao Z, Liu Q, Liu Q (2020) A 2D hydrodynamic model for shallow water flows with significant infiltration losses. *Hydrol Process* 34:2263–2280
- Özgen I, Simons F, Zhao J, Hinkelmann R (2014) Modeling shallow water flow and transport processes with small water depths using the hydroinformatics modelling system. CUNY Academic Works, New York
- Rawls W, Brakensiek D, Miller N (1983) Green-Ampt infiltration parameters from soils data. *J Hydraul Eng* 1:62–70
- Rawls WJ, Brakensiek DL, Simanton JR, Kohl KD (1990) Development of a crust factor for a Green Ampt Model. *Trans ASAE* 33(4):1224–1228. <https://doi.org/10.13031/2013.31461>
- Sharma M, Gander G, Hunt C (1980) Spatial variability of infiltration in a watershed. *J Hydrol* 45 (1–2):101–122
- Simons F, Busse T, Hou J, Özgen I, Hinkelmann R (2012) HMS: model concepts and numerical methods around shallow water flow within an extendable modeling framework. In: Proceedings of the 10th international conference on hydroinformatics, Hamburg



- Simons F, Busse T, Hou J, Özgen I, Hinkelmann R (2014) A model for overland flow and associated processes within the hydroinformatics modelling system. *J Hydroinformatics* 16 (2):375–391
- Smith L, Liang Q, James P, Lin W (2017) Assessing the utility of social media for flood risk management. *J Flood Risk Manage* 10:370–380. <https://doi.org/10.1111/jfr3.12154>
- Starkey E, Parkin G, Birkinshaw S, Large A, Quinn P, Gibson C (2017) Demonstrating the value of community-based ('citizen science'). *J Hydrol* 548:801–817
- Tackett J, Pearson RW (1965) *Soil science*
- Tügel F, Özgen I, Hadidi A, Tröger U, Hinkelmann R (2018) Modelling of flash floods in wadi systems using a robust shallow water model—case study El Gouna, Egypt. In: *Advances in hydroinformatics*. Singapore, Springer
- Tügel F, Özgen-Xian I, Marafini E, Hadidi A, Hinkelmann R (2020a) Flash flood simulations for an Egyptian city—mitigation measures and impact of infiltration. *Urban Water J* 14(5):396–406
- Tügel F, Abdelrahman A, Özgen-Xian I, Hadidi A, Hinkelmann R (2020b) Rainfall-runoff analysis of the Wadi Bili catchment in the Red Sea Governorate of Egypt. In: *Advances in hydroinformatics*. Springer, Singapore
- Vergoesen T, Verschelling E, Becker B (2014) Modelling of sustainable urban drainage measures. *Revista De Ingenieria Innova* 8:1–16
- Whisler F, Bouwer H (1970) Comparison of methods for calculating vertical drainage and infiltration for soils. *J Hydrol* 1:1–19
- Xing Y, Liang Q, Wang G, Ming X, Xia X (2019) City-scale hydrodynamic modelling of urban flash floods: the issues of scale and resolution. *Nat Hazards* 96:473–496
- Yu D, Yin J, Liu M (2016) Validating city-scale surface water flood modelling using crowdsourced. *Environ Res Lett* 11(12):124011

**Open Access** This chapter is licensed under the terms of the Creative Commons Attribution 4.0 International License (<http://creativecommons.org/licenses/by/4.0/>), which permits use, sharing, adaptation, distribution and reproduction in any medium or format, as long as you give appropriate credit to the original author(s) and the source, provide a link to the Creative Commons license and indicate if changes were made.

The images or other third party material in this chapter are included in the chapter's Creative Commons license, unless indicated otherwise in a credit line to the material. If material is not included in the chapter's Creative Commons license and your intended use is not permitted by statutory regulation or exceeds the permitted use, you will need to obtain permission directly from the copyright holder.

